Distribution pattern of metal atoms in bimetal-doped pyridinic-N_4 pores determines their potential for electrocatalytic N_2 reduction

The distribution pattern of metal atoms in bi-metal doped pyridinic-N_4 pores determines their potential for electrocatalytic N_2 reduction

Parisa Nematollahi[*a], Erik C. Neyts[a]

[a] Research Group Plasmant, NANO lab Center of Excellence, Department of Chemistry, University of Antwerp, Universiteitsplein 1, 2610 Antwerp, Belgium

* Corresponding author. **Phone:** (+32) 32652346. **E-mail**: parisa.nematollahi@uantwerpen.be

Abstract

Doping two single transition metal (TM) atoms on a substrate host open numerous possibilities for catalyst design. But what if the substrate contains more than one vacancy site? Then, the combination of two TMs along with their distribution patterns becomes a design parameter potentially complementary to the substrate itself and the bi-metal composition. In this study, we investigate ammonia synthesis under mild electrocatalytic conditions on a transition metal-doped porous $C_{24}N_{24}$ catalyst using density functional theory (DFT). The TMs studied include Ti, Mn, and Cu in a 2:4 dopant ratio ($Ti_2Mn_4@C_{24}N_{24}$ and $Ti_2Cu_4@C_{24}N_{24}$). Our computations show that a single Ti atom in both catalysts exhibits the highest selectivity for N_2 fixation at ambient conditions. This work is a good theoretical model to establish the structure-activity relationship and the knowledge earned from the metal-N_4 moieties may help studies of related nanomaterials especially those with curved structures.

Keywords: Nitrogen reduction, pyridinic nitrogen, fullerene, bi-metal doping, N_2 fixation, $C_{24}N_{24}$

Introduction

Ammonia (NH_3) is a key chemical in the production of fertilizers, and ammonia synthesis is, therefore, a key industrial process. The primary method for ammonia synthesis is the thermal catalytic Haber-Bosch process, using approximately 1 – 2% of the current global energy production [1-3]. To reduce this enormous energy cost, other methods are actively investigated, including plasma catalysis [4] and electrocatalysis [5, 6]. In recent years, a great number of investigations were carried out on electrochemical methods using various electrocatalysts [7-12]. Among these approaches, electrocatalytic nitrogen reduction reaction (NRR) can be a practical solution to form ammonia using electrical energy produced from solar or wind sources [13-15]. This method is highly promising because it can be carried out under ambient conditions using low-cost aqueous electrolytes as a proton source instead of pure H_2 gas [16-18]. A remaining key issue, however, is the development of suitable electrocatalysts to accelerate the N_2 fixation reaction, increasing the NH_3 selectivity and decreasing the overpotential [19, 20].

To date, numerous catalysts have been fabricated. However, many efforts focused solely on metal-based catalysts, and therefore metal-free or single metal atom catalysts have so far been only rarely explored. Considering that single metal atom catalysts carry the potential of excellent activity, selectivity, stability, and free from poisoning effects in addition to low cost and environmental friendliness [21-24], the design and development of these catalysts for NRR are of great interest [25, 26].

Porous carbon-based catalysts are widely used as support materials in heterogeneous catalysis [27-31]. The archetypical example is the C_{60} fullerene, which can be synthesized with a highly defective surface and abundant holes allowing for easy doping [32, 33]. Indeed, the chemical inertness of pure fullerenes prevents their possible application for catalytic reactions. Thus, doping C_{60} with single transition metal (TM) atoms yielding compounds such as $C_{58}Pt$ and $C_{59}Pt$ [34], modify its electronic structure such that it becomes chemically active.

Furthermore, C_{60} co-doped by single TM and heteroatoms, especially nitrogen, also gained significant interest [35, 36]. The excellent performance of TM-doped-based catalysts can be attributed to the coexistence of empty and occupied d-orbitals, which can both accept the lone electron pair of N_2 and donate electrons into the antibonding orbitals of N_2 to weaken the triple N≡N bond [37]. Upon heteroatom doping, such as nitrogen doping, the carbon π electrons are activated by conjugating with the lone-pair electrons from N. Thus, the C atoms neighboring N become active centers for catalytic reactions. However, one of the main challenges in the synthesis of TM-C_{60} is the aggregation of metal atoms [38, 39].

Recently, extensive efforts are done in developing single site catalysts such as pyrolyzed TM-modified nitrogenated complexes (TM=Fe, Co, Mn, Cr, Ni) [40-50] which can be used in various applications such as Oxygen Reduction Reaction (ORR) and batteries [12, 43, 51-54]. The single TM atom doped in these pyridinic nitrogen-doped graphene units was firmly fixed preventing the metal aggregation. Amongst these structures, porous $C_{24}N_{24}$ is of great interest as a truncated N-doped C_{60} nanocage that can be implemented in catalytic reactions such as CO oxidation [55, 56] or NO reduction [57]. The $C_{24}N_{24}$ fullerene has six N_4 cavities with eight s-triazine rings which are connected via C-C bonds. Each N_4 cavity of $C_{24}N_{24}$ can host a single TM atom. Recently, TM-doped $C_{24}N_{24}$ and $C_{24}B_{24}$ fullerenes were studied for hydrogen storage [58-60], ORR [61], and gas conversion [55].

In our previous study [62], we investigated the effects of various distribution patterns of two different TM atoms in six N_4 cavities of a $C_{24}N_{24}$ cage ($Ti_xCu_z@C_{24}N_{24}$, $Ti_xMn_y@C_{24}N_{24}$, and $Cu_zMn_y@C_{24}N_{24}$, x,y,z = 0-6) on their geometric, thermodynamic, and electronic properties. Also, we investigated the selectivity of doped atoms toward gas adsorption (N_2, CO_2, H_2, and NO_2). We found that $Ti_2Mn_4@C_{24}N_{24}$ and $Ti_2Cu_4@C_{24}N_{24}$ with a TM1:TM2 ratio of 2:4 are the two most energetically favorable configurations for gas capture.

In the current study, we carry out a comprehensive investigation of NRR on each metal active

site, Ti/Mn and Ti/Cu, of $Ti_2Mn_4@C_{24}N_{24}$ and $Ti_2Cu_4@C_{24}N_{24}$, respectively, to obtain insight into the atomic-scale performance of these bi-metal catalysts with different atom distributions in NRR. All three dissociative mechanisms of N_2 on each metal center followed by their associated pathways, onset potentials, and overpotentials, are thoroughly explored. Our results provide a further understanding of the factors beyond charge transfer and catalytic activity of double atom catalysts. W confirm that the distribution patterns of bi-metal into the pyridinic-N_4 vacancies of carbon nitride nanomaterials play a key role in their catalytic activity which may enable their application for sustainable NH_3 formation.

Computational details

DFT method. All calculations were carried out using the Vienna ab initio simulation package (VASP) [63-65]. The ion-electron interactions are described by the projected augmented wave (PAW) method [66]. The Perdew-Burke-Ernzerhof (PBE) [67] functional is used for exchange and correlation. Convergence of the plane-wave cutoff energies was checked and cutoff energy of 400 eV is chosen and employed in all calculations. Partial occupancies are addressed using Gaussian smearing with a smearing width of 0.05 eV. The zero-damping Grimme approximation, DFT + D_2, is used to compute the weak dispersion interactions [68]. All calculations are spin-polarized. The convergence criterion for the residual force and energy in structural relaxations was set to 0.01 eV/Å and 10^{-6} eV, respectively. To avoid self-interaction through the periodic boundaries, a 16 × 16 × 20 Å supercell is used and the positions of all the atoms are fully relaxed during the optimization. The basic structure of fullerene is taken from American Mineralogist Crystal Structures Database [69]. Atomic charges and charge transfer were calculated from the Bader charge scheme [70].

To estimate the stability of the embedded TM atom in the defective structure [71] we calculated the binding energy of doped metal atoms (Ti, Mn, or Cu) into the pyridinic-N_4 cavities of $C_{24}N_{24}$ in $Ti_2Mn_4@C_{24}N_{24}$ and $Ti_2Cu_4@C_{24}N_{24}$ complexes. Since there are 6 metal atoms doped in each

configuration, we calculated the binding energy of each atom separately:

$$E_b = E_{A2B4@C24N24} - E_{A1B4@C24N24 \text{ or } A2B3@C24N24} - E_{A \text{ or } B} \quad (1)$$

where the $E_{A2B4@C24N24}$ is the total energy of $Ti_2Mn_4@C_{24}N_{24}$ or $Ti_2Cu_4@C_{24}N_{24}$ complex. $E_{A1B4@C24N24 \text{ or } A2B3@C24N24}$ is the total energy of $Ti_1Mn_4@C_{24}N_{24}$, $Ti_2Mn_3@C_{24}N_{24}$ or $Ti_1Cu_4@C_{24}N_{24}$, $Ti_2Cu_3@C_{24}N_{24}$. The $E_{A \text{ or } B}$ corresponds to the energy of a single metal atom. The adsorption energy is defined as $\Delta E_{ads} = \Delta E_{AS} - \Delta E_S - \Delta E_A$ where ΔE_{AS}, ΔE_S, and ΔE_A are the energy of the adsorbed species on the substrate, the energy of the substrate, and the energy of the adsorbate, respectively. To find out the reliability of our calculations, the geometric parameters of H_2 and fullerene are computed and compared with experimental data. The calculated binding energy and bond length of H_2 were 4.53 eV and 0.75 Å, which are close to the reported experimental values of 4.53 eV and 0.74 Å. According to our computations, the C-C bond lengths in C_{60} are 1.44 Å and 1.40 Å, respectively. These values are in good agreement with the reported experimental data i.e. 1.43-1.46 Å [72]. Therefore, we can confirm that our calculations are sufficiently accurate to be compared with other experimental or theoretical investigations. The full details of the computational hydrogen electrode (CHE) model, zero-point energies, and entropy of the reaction intermediates are explained in the Supporting Information.

Results and discussions

Screening the geometry and stability of TM@$C_{24}N_{24}$ nanocages

The porous $C_{24}N_{24}$ is formed by removing the 12 C atoms in C_{60} that connect two pentagons, creating 6 di-vacancies, (indicated with red circles), as shown in Figure 1. Subsequently, four undercoordinated C-atoms are substituted with N-atoms, creating six pyridinic-N_4 cavities and eight connected s-triazine rings with C−C and C−N bond lengths of 1.55 Å and 1.34 Å, respectively. These nitrogenated vacancies can host various TM atoms providing various active centers. The calculated cohesive energy per atom in $C_{24}N_{24}$ is quite high, viz. E_{coh} = -7.81 eV.

We define the cohesive energy as E_{coh} = 1/48[E_{C24N24} - 24E_C - 24E_N], where E_{C24N24}, E_C, and E_N are the energy of pristine $C_{24}N_{24}$, a single C and N atom, respectively. This value agrees satisfactory with that reported by Ghosh et. al (-7.40 eV) [73] while it is significantly higher than the value reported by Tang et al. (-5.78 eV) [59]. The HOMO-LUMO gap of $C_{24}N_{24}$ is calculated to be E_g = 2.82 eV, which is similar to the value reported by Ma et al. [60], Song et al. [74], and is higher than the value reported in other investigations [61, 73].

We consider a combination of two metal atoms from the selected atoms, Ti, Mn, and Cu transition metals, i.e., TiCu, TiMn, and MnCu. Then, various distribution patterns of these atoms into the six pyridinic-N_4 $C_{24}N_{24}$ cavities were generated, whereas the $Ti_2Mn_4@C_{24}N_{24}$ and $Ti_2Cu_4@C_{24}N_{24}$ structures showed better catalytic activity for gas adsorption. Upon doping, Ti, Mn, and Cu atoms slightly protrude from the cage due to their larger atomic radius as reported in previous investigations [73, 75] (see Figure 1). To assess the stability of the modified complexes, the binding energy of each metal atom in each configuration was calculated. In all the cases, the binding energy of Ti atom in $Ti_1Mn_4@C_{24}N_{24}$ ($E_{b\text{-}Ti}$=−7.77 eV) and $Ti_1Cu_4@C_{24}N_{24}$ ($E_{b\text{-}Ti}$=−7.80 eV) structures outcompete the binding energy of Mn atom in $Ti_2Mn_3@C_{24}N_{24}$ ($E_{b\text{-}Mn}$=−4.97 eV) and Cu atoms in $Ti_2Cu_3@C_{24}N_{24}$ ($E_{b\text{-}Cu}$ =−4.01 eV). According to the Bader charge analysis, all doped TMs are positively charged (see Table S1 of the Supporting Information). Although Ti atoms have the highest charge transfer in both $Ti_2Mn_4@C_{24}N_{24}$ and $Ti_2Cu_4@C_{24}N_{24}$ catalysts, the charge depletion on these atoms in $Ti_2Cu_4@C_{24}N_{24}$ is about |0.06| e higher than that of $Ti_2Mn_4@C_{24}N_{24}$. The charge transfer from Ti to the cage leads to the Ti-N bond elongation (2.04 Å) which is higher than those of Mn-N (1.98 Å) and Cu-N (1.97 Å). The charge density difference (CDD) map is provided in Figure 1b. Thus, as demonstrated here and in our previous report [62], the TMs anchored $C_{24}N_{24}$ substrate is stable enough to effectively catalyze NRR.

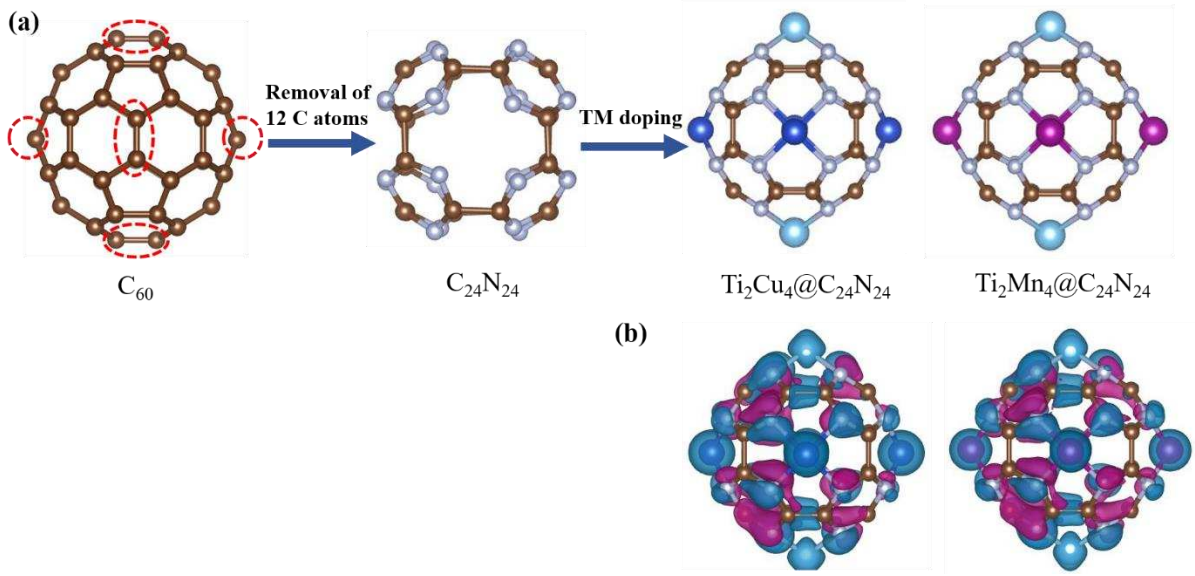

Figure 1. (a) schematic presentation of truncation substantial doping of C_{60} to generate $C_{24}N_{24}$ and consequently bi-metal doped $C_{24}N_{24}$, (b) The optimized charge density difference (CDD) for $Ti_2Mn_4@C_{24}N_{24}$ and $Ti_2Cu_4@C_{24}N_{24}$ where $\Delta\rho = \rho_{(substrate+ads)} - \rho_{(substrate)} - \rho_{(ads)}$. In the CDD map dark purple shows the negative charge accumulation and dark blue color represent the positive charge depletion areas. The isosurface level was set to 0.06 e/Bohr^3. Atom color code: brown, C; blue, Ti; light blue, N; purple, Mn; dark blue, Cu.

Activation of N_2 on bi-metal doped $C_{24}N_{24}$ cages

We first study N_2 chemisorption on the catalyst surface. All the adsorption energies are calculated considering the zero-point energy correction. While the adsorption of N_2 is the first step for NRR, its adsorption pattern (i.e. end-on or side-on orientation) is an important factor for the further hydrogenation steps, which were reported in previous studies [76-79]. The optimized structures along with the corresponding adsorption energies of N_2 on $Ti_2Mn_4@C_{24}N_{24}$ and $Ti_2Cu_4@C_{24}N_{24}$ are shown in Figures 2 a-d and e. The adsorption free energy of N_2 is shown in Figure 2f.

The anchored TMs have both unoccupied and occupied d-orbitals which can accept electrons via σ-donation, and donate electrons via π back-donation. The latter increases the occupation of the antibonding orbitals of N_2, weakening the triple bond [37]. Additionally, the strongly-polarized covalent bond between one TM atom and one (in end-on mode) or two N atoms (in side-on mode), is accompanied by a charge transfer from TM to antibonding orbitals of N_2 as

well as the elongation of N–N bond by about 5%. This is also confirmed by comparing the CDD of the pure catalyst before and after N_2 adsorption, as depicted in Figures 1 and 2a-d.

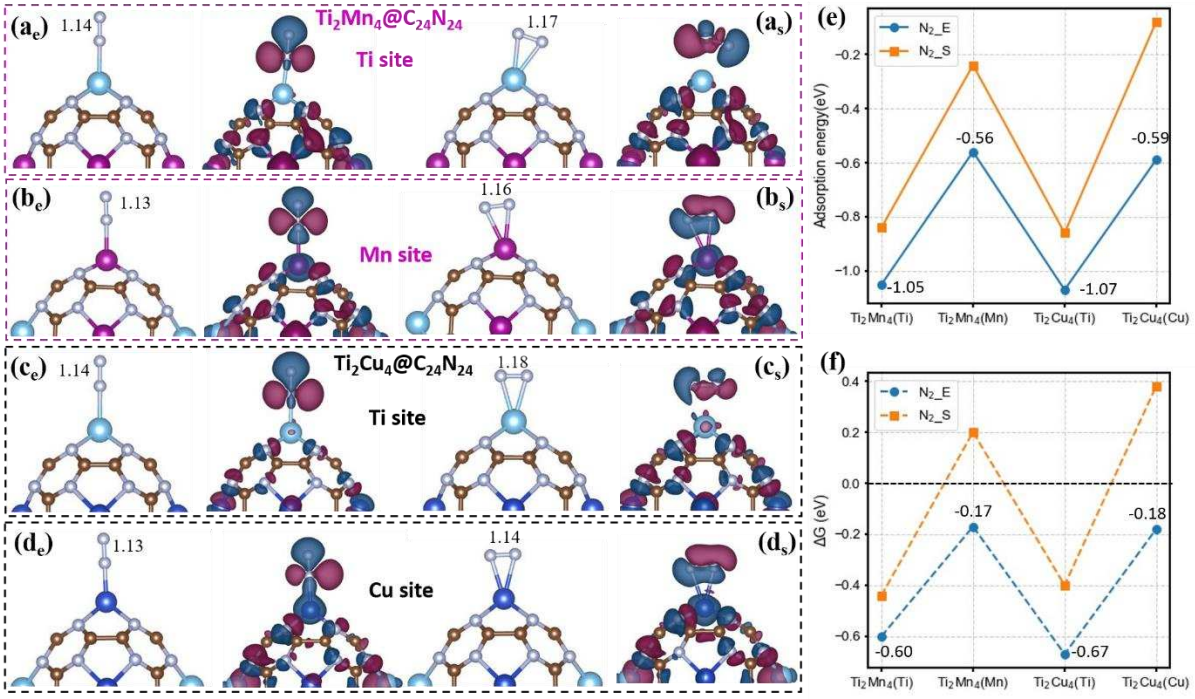

Figure 2. Optimized configurations of end-on and side-on N_2 adsorption on Ti (Mn) site of $Ti_2Mn_4@C_{24}N_{24}$ (a and b), and Ti (Cu) site of $Ti_2Cu_4@C_{24}N_{24}$ (c and d) along with their corresponding charge density difference (CDD). e and s suffixes refer to the end-on and side-on adsorption modes, respectively. In the CDD map, dark purple shows negative charge accumulation and dark blue color represents the positive charge depletion areas. The isosurface level was set to 0.04 e/Bohr^3 (e) The computed energy and (f) free energy of end-on and side-on N_2 adsorption. The values that are shown above each dot are the calculated energy of adsorption in eV. All bond lengths are in Å. Color code: brown, C; blue, Ti; light blue, N; purple, Mn; dark blue, Cu.

Moreover, the increased charges and N-N bond elongation demonstrate that the occupied d-orbitals of isolated metal atoms can donate electron density to the antibonding π^* orbitals of adsorbed N_2. The calculated absolute Bader charges (see Table S1) versus the N-N bond length for both end-on and side-on configurations are plotted in Figure 3. Although the charge transfer is about $|0.1|$ e higher in the side-on configurations of N_2 than the end-on configuration, it has no significant effect on their corresponding adsorption energies. The Cu atom of the $Ti_2Cu_4@C_{24}N_{24}$ catalyst is an exception with $|0.02|$ e higher charge transfers in the end-on orientation which can be related to the filled d-orbitals of the Cu atom.

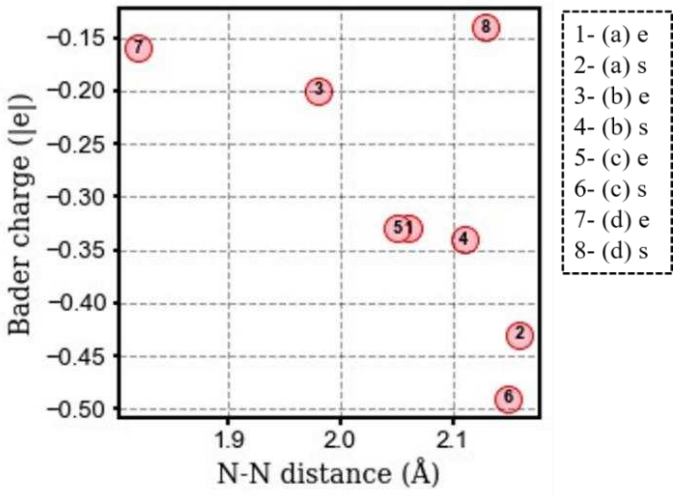

Figure 3. Relationship between Bader charges of adsorbed N_2 and N–N bond lengths. (a-d) are the complexes are shown in Figure 2 and e and s stands for end-on and side-on N_2 configuration.

According to the definition of adsorption energy, a negative E_{ads} indicates exothermic adsorption and stable configuration [80]. One can see that in both catalysts, the adsorption energy (E_{ads}) and the thermodynamic feasibility of N_2 adsorption (ΔG_{N2}) with the end-on orientation on the Ti atom are more negative than that on the Mn and Cu atoms (see Figures 2e and 2f).

The mechanisms of electrocatalytic NRR

Electrocatalytic NRR proceeds at the cathode with six hydrogenation steps, which can be described as $N_2 + 6H^+ + 6e^- \rightarrow 2NH_3$. The NRR starts with the adsorption of molecular nitrogen on the active sites through either end-on or side-on configurations forming an $*N_2$ intermediate, as discussed above. Then, the subsequent hydrogenation of $*N_2$ occurs. The addition of hydrogen to the surface represents a combination of a proton supplied from the solvent and an electron from the electrode surface. The NRR mechanisms have been widely investigated and well-established over time as presented in Scheme 1 [6, 81-85]. The reaction mechanisms are divided into three different pathways, including the distal or alternating reaction pathways for end-on configuration [85, 86] and the enzymatic pathway for side-on configuration. In the distal mechanism, the H^+/e^- pairs first attack one *N atom preferentially to produce the first NH_3 and

then interact with another *N atom for the formation of the second NH_3. In the alternating pathway, the H^+/e^- pairs attack two *N atoms of the end-on adsorbed *N_2 alternately. In contrast, the two N atoms of the adsorbed side-on *N_2 configuration are hydrogenated by the H^+/e^- pairs, alternately in the enzymatic route. The corresponding NRR reactions are listed in Table 1.

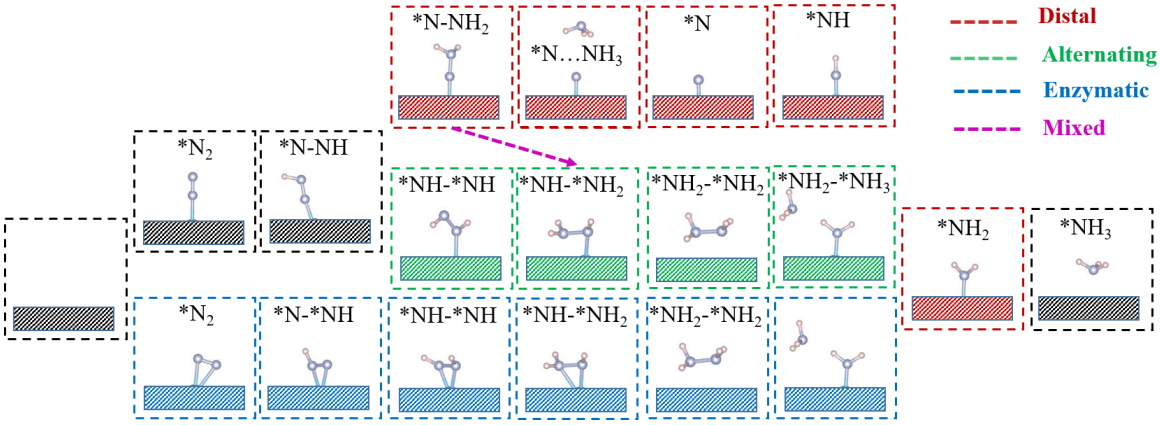

Scheme 1. Schematic representative of possible pathways for NRR on $Ti_2Mn_4@C_{24}N_{24}$ and $Ti_2Cu_4@C_{24}N_{24}$.Color code: light blue, N; White, H.

Table 1. The sub-reactions of distal, alternating, and enzymatic mechanisms

mechanism	Reactions	
Distal	*+ 6 (H^++ e^-) + N_2 → *N_2 + 6 (H^++ e^-)	(2)
	*N_2 + 6 (H^++ e^-) → *N-NH + 5 (H^++ e^-)	(3)
	*N-NH + 5 (H^++ e^-) → *N-NH_2 + 4 (H^++ e^-)	(4)
	*N-NH_2 + 4 (H^++ e^-) → *N + NH_3(g) + 3 (H^++ e^-)	(5)
	*N + 3 (H^++ e^-) → *NH + 2 (H^++ e^-)	(6)
	*NH + 2 (H^++ e^-) → *NH_2 + (H^++ e^-)	(7)
	*NH_2 + (H^++ e^-) → *NH_3	(8)
	*NH_3 → * + NH_3	(9)
Alternating & Enzymatic	*+ 6 (H^++ e^-) + N_2 → *N_2 + 6 (H^++ e^-)	(2)
	*N_2 + 6 (H^++ e^-) → *N-NH + 5 (H^++ e^-)	(10)
	*N-NH + 5 (H^++ e^-) → *NH-*NH + 4 (H^++ e^-)	(11)
	*NH-*NH + 4 (H^++ e^-) → *NH-*NH_2 + 3 (H^++ e^-)	(12)
	NH-NH_2 + 3 (H^++ e^-) → *NH_2-*NH_2 + 2 (H^++ e^-)	(13)
	NH_2-NH_2 + 2 (H^++ e^-) → *NH_2 + NH_3 + (H^++ e^-)	(14)
	*NH_2 + (H^++ e^-) → *NH_3	(8)
	*NH_3 → * + NH_3	(9)

One can see in scheme 1 and Table 1 that the formation of the first NH_3 molecule depends on the different reaction pathways. In addition, the first hydrogenation step ($*N_2+H^+ + e^- \rightarrow *NNH$) and the last hydrogenation step ($*NH_2+H^+ + e^- \rightarrow *NH_3$) in all pathways are the same and are the most likely rate-determining step for the whole NRR process [5, 87, 88]. Therefore, rapid screening of these two steps is widely used to determine the best NRR catalysts. To achieve this, we calculated the free energy changes of the first and last electrochemical hydrogenation steps on $Ti_2Mn_4@C_{24}N_{24}$ and $Ti_2Cu_4@C_{24}N_{24}$ considering both end-on (distal and alternating pathways) and side-on configurations (enzymatic pathway). The obtained results are shown in Figure 4. One can see that the first hydrogenation of $*N_2$ on Ti, Mn, and Cu active sites in both catalysts is uphill, and hence not spontaneous at room temperature. The higher ΔG values are for distal and alternating mechanisms, especially on the Mn (Cu) atom of $Ti_2Mn_4@C_{24}N_{24}$ ($Ti_2Cu_4@C_{24}N_{24}$). The last hydrogenation step on the Ti atom of $Ti_2Mn_4@C_{24}N_{24}$ and $Ti_2Cu_4@C_{24}N_{24}$ is endothermic while it is exothermic on the Mn (Cu) atom of $Ti_2Mn_4@C_{24}N_{24}$ ($Ti_2Cu_4@C_{24}N_{24}$).

In the next step, based on the screening results, we investigated the NRR on the Ti atom in both catalysts since it shows the strongest stabilization for N_2 adsorption and has lower ΔG values for the first hydrogenation step. Therefore, here we only focus on the detailed NRR mechanisms over the Ti atom in $Ti_2Mn_4@C_{24}N_{24}$ and $Ti_2Cu_4@C_{24}N_{24}$. Mn and Cu atoms require a high free energy value for $*N_2$ hydrogenation to *NNH which hinders the NRR to proceed and thus can be neglected. However, to further estimate and compare the catalytic activity and the selectivity of each dopant for NRR, we then calculated the NRR reaction steps on Mn and Cu. These feasible reaction pathways and the corresponding reaction energies are given in the Supporting Information.

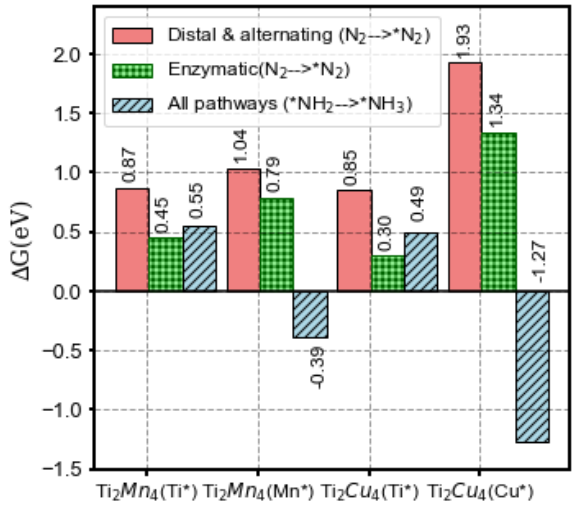

Figure 4. The calculated changes of the Gibbs free energy of the first and last hydrogenation steps of NRR over Ti(Mn), and Ti(Cu) active sites of $Ti_2Mn_4@C_{24}N_{24}$ and $Ti_2Cu_4@C_{24}N_{24}$, respectively.

Mechanisms of the NRR on $Ti_2Mn_4@C_{24}N_{24}$

One of the advantages of bi-metal catalysts is to provide two active sites with different ratios for entering into a chemical or electrochemical reaction. Using $Ti_2Mn_4@C_{24}N_{24}$ as a catalyst, the presented active sites are Ti and Mn. Since Ti has strong adsorption to N_2, we only focus on the distal and alternating NRR mechanisms on this active site.

Starting from the end-on N_2 adsorption on the Ti atom of $Ti_2Mn_4@C_{24}N_{24}$ through the distal pathway, the adsorbed *N_2 will be hydrogenated by a $H^+ + e^-$ transfer to *NNH species adsorbed on the Ti site (see Figure 5a) and the N-N bond is elongated from 1.12 Å in the gas phase to 1.23 Å. This elementary step is slightly uphill in the free energy profile and is the potential determining step (PDS) with the ΔG_{max} = 0.87 eV. The next hydrogenation step and formation of *NNH_2 is downhill with $\Delta G = -0.19$ eV. Subsequently, the first NH_3 molecule is released in the third protonation step and one *N atom remains on the Ti site of $Ti_2Mn_4@C_{24}N_{24}$. According to the calculated free energies, the formation of the first NH_3 molecule is endergonic with ΔG = 0.48 eV. The subsequent hydrogenation steps to form the second *NH_3 molecule are all downhill except for the formation of the second *NH_3 which is uphill by ΔG=0.55 eV. The removal of *NH_3 from the Ti atom in $Ti_2Mn_4@C_{24}N_{24}$ needs to overcome free energy of 0.85

which might vary depending on each catalyst and the related mechanism. However, according to the experimental data, the energy of this process is not considered a PDS and is exergonic under acidic conditions because the adsorbed $*NH_3$ converts to NH_4^+ by reacting with H^+ in an acidic electrochemical environment, and does not directly desorb from the surface to form gaseous NH_3 [89, 90]. Furthermore, the energy released in the hydrogenation process can overcome the energy required to release the second $*NH_3$ molecule from the surface (see Figure 5). The calculated onset potential for the distal pathway on the Ti atom of $Ti_2Mn_4@C_{24}N_{24}$ is $U_{lim} = -\Delta G_{max}/e = -0.87$ V vs. the RHE. The overpotential (η) is known as a good indicator of catalytic reactivity. A smaller η value indicates a faster N_2 reduction reaction. The overpotential for the distal mechanism on the Ti center is calculated to be $0.09 - (-0.87) = 0.96$ V.

When the NRR follows the alternating pathway, the protonation alternately occurs between the two N atoms, resulting in the release of the first NH_3 at the sixth step and desorbs into the solution (Scheme 1). The PDS of N_2 fixation on the Ti site of $Ti_2Mn_4@C_{24}N_{24}$ in the alternating pathway is the formation of hydrazine (N_2H_4) with the maximum ΔG value of 0.89 eV, about 0.02 eV higher than that of the first protonation step. The hydrogenation of $*NH_2$ species also results in the non-electroactive release of the second $*NH_3$ molecule. Therefore the calculated onset potential is $U_{lim} = -0.89$ V vs. the RHE with an overpotential of 0.98 V.

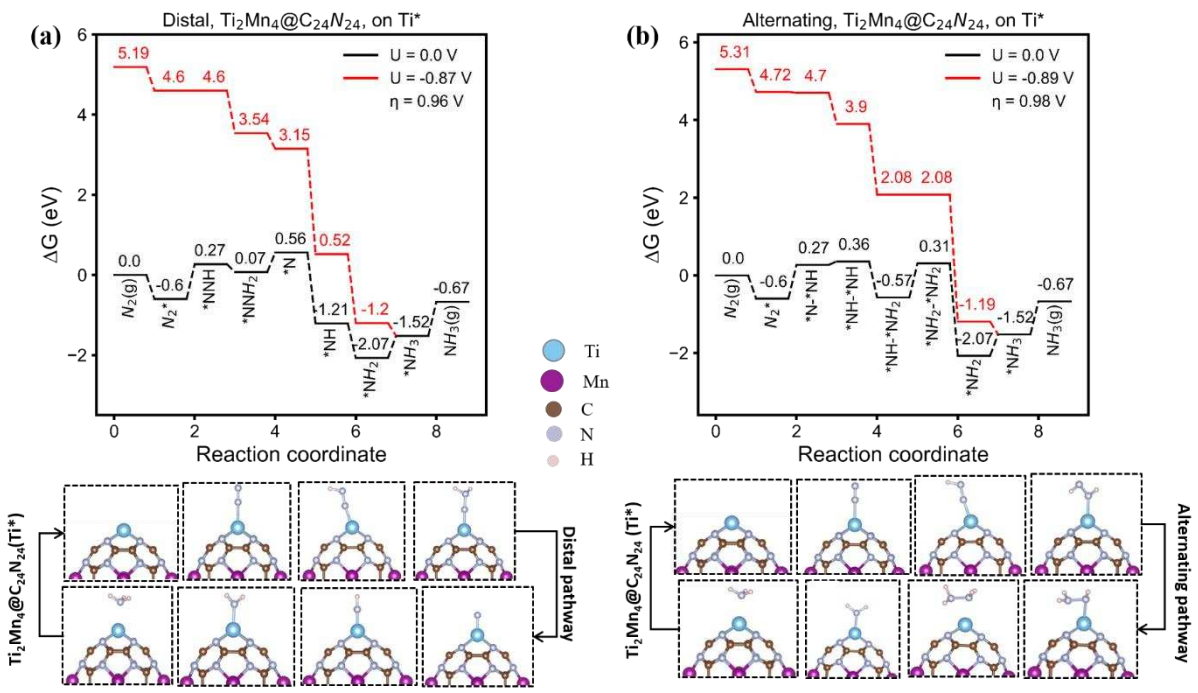

Figure 5. NRR via distal(a) and alternating (b) mechanisms on the Ti site of $Ti_2Mn_4@C_{24}N_{24}$ along with the corresponding optimized configurations at zero and applied potential.

Mechanisms of NRR on $Ti_2Cu_4@C_{24}N_{24}$

To evaluate the reductive performance of electrocatalytic NRR on $Ti_2Cu_4@C_{24}N_{24}$ we calculated the limiting potential for all mechanisms considering the Ti atom as the active center. Providing that the NRR follows the distal pathway on the Ti center of $Ti_2Cu_4@C_{24}N_{24}$, the adsorbed N_2 will be hydrogenated by adsorbing a proton-coupled with an electron transfer and form a *NNH species with a lower ΔG value of 0.85 eV than that on Ti atom of the $Ti_2Mn_4@C_{24}N_{24}$ (see Figure 6a). In the following step, the $H^+ + e^-$ consecutively attacks the N atom of the *NNH species. As a result, the $*NNH_2$ species is yielded and the Gibbs free energy decreases by -0.14 eV. Subsequently, the first NH_3 molecule can be released after the interaction of the third $H^+ + e^-$ with the $*NNH_2$ group in an endothermic reaction (ΔG=0.60 eV), and one *N atom remains on the Ti atom. In the subsequent exergonic steps, the remaining *N species will be hydrogenated to the second $*NH_3$ from which the last protonation step is uphill by ΔG=0.49 eV. Remarkably, in this distal pathway, the protonation of N_2 to form *NNH

species is the potential-limiting step due to the maximum ΔG values (0.85 eV) among all elementary steps.

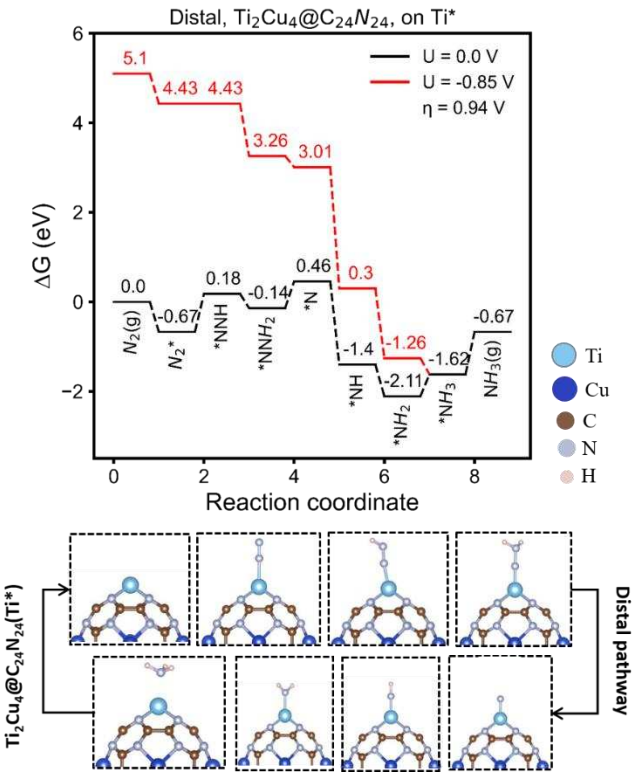

Figure 6. NRR via distal mechanisms on Ti site of $Ti_2Cu_4@C_{24}N_{24}$ along with the corresponding optimized configurations.

We also evaluated the NRR through alternating and enzymatic pathways on Ti sites of $Ti_2Cu_4@C_{24}N_{24}$. Our results show that the formation of hydrazine species in both the alternating and enzymatic pathways, *NH-*NH_2 + (H^++ e^-) → *NH_2-*NH_2, can be identified as the PDS with ΔG_{max} = 1.01 and 0.97 eV, corresponding to the limiting potential of -1.01 and -0.97 V vs. RHE, respectively (see Figure S4). Therefore, we believe that these mechanisms are unfavorable for NRR. As mentioned before, we showed that the Cu center of $Ti_2Cu_4@C_{24}N_{24}$ is not active for NRR due to the thermodynamically high free energy value required for the first hydrogenation of *N_2 species. The full details of the corresponding reaction coordinates along with the optimized configurations are provided in the Supporting Information.

Recently, a new pathway was proposed for N_2 reduction, the so-called mixed pathway [91, 92].

In this pathway, the *NNH_2 species is formed first, through the distal pathway. Subsequently, the next hydrogenation reaction forming *NH-*NH_2 proceeds through the alternating pathway. This is shown by the dotted purple line in Scheme 1. Thus, we also investigated this hybrid mechanism on the active centers of both $Ti_2Mn_4@C_{24}N_{24}$ and $Ti_2Cu_4@C_{24}N_{24}$ catalysts. We find that the onset potential of the mixed pathway on Ti (Mn) of $Ti_2Mn_4@C_{24}N_{24}$ and Ti (Cu) of $Ti_2Cu_4@C_{24}N_{24}$ is -0.89 (-1.04 V) and -1.01 (-1.93 V), respectively. Since the obtained onset potential value in the mixed pathway is higher than that reported in the paper, we conclude that this mechanism is not energetically more favorable for NRR on $Ti_2Mn_4@C_{24}N_{24}$ and $Ti_2Cu_4@C_{24}N_{24}$. In addition, Ti sites in both catalysts can actively catalyze the NRR due to the lower onset potential of -0.87 and -0.85 V vs. RHE.

Screening the computed limiting potentials for various NRR mechanisms on $Ti_2Mn_4@C_{24}N_{24}$ and $Ti_2Cu_4@C_{24}N_{24}$ we find that the selectivity of Ti sites in $Ti_2Mn_4@C_{24}N_{24}$ for NRR through the distal and alternating mechanisms and in $Ti_2Cu_4@C_{24}N_{24}$ through the distal mechanism is higher than those on the Mn and Cu centers.

Competition between NRR and HER on $Ti_2Mn_4@C_{24}N_{24}$ and $Ti_2Cu_4@C_{24}N_{24}$

The hydrogen evolution reaction (HER, $2H^+ + 2\ e^- \rightarrow H_2$, $E^0 = 0$ V) is the key side reaction during the NRR. This reaction consumes a significant amount of H^+/e^- pairs, and in the acidic conditions might occupy the same active sites of NRR electrocatalysts and produce H_2 molecules at similar limiting potentials as for NRR, reducing the Faraday efficiency (FE) and inducing low selectivity [93, 94]. Therefore, as the main competitor to NRR, HER should be suppressed to improve the selectivity of nitrogen fixation [95]. As shown in Figure 2, we found that N_2 can strongly adsorb on the surface. We then assess the competition between the activation of N_2 and the first step of HER assuming the Volmer mechanism ($H^+ + e^- \rightarrow$ *H) by calculating their adsorption Gibbs free energies [24, 96] shown in Figure 7a. Regardless of the N_2 adsorption mode (side-on or end-on), the metal active sites are selective towards adsorption

of N_2 rather than *H adsorption. However, although the adsorption Gibbs free energy of *H on Ti atom of $Ti_2Cu_4@C_{24}N_{24}$ is negative, the N_2 adsorption in end-on mode has still the higher negative value indicating that the metal atoms possess potential functionality for catalyzing NRR over HER.

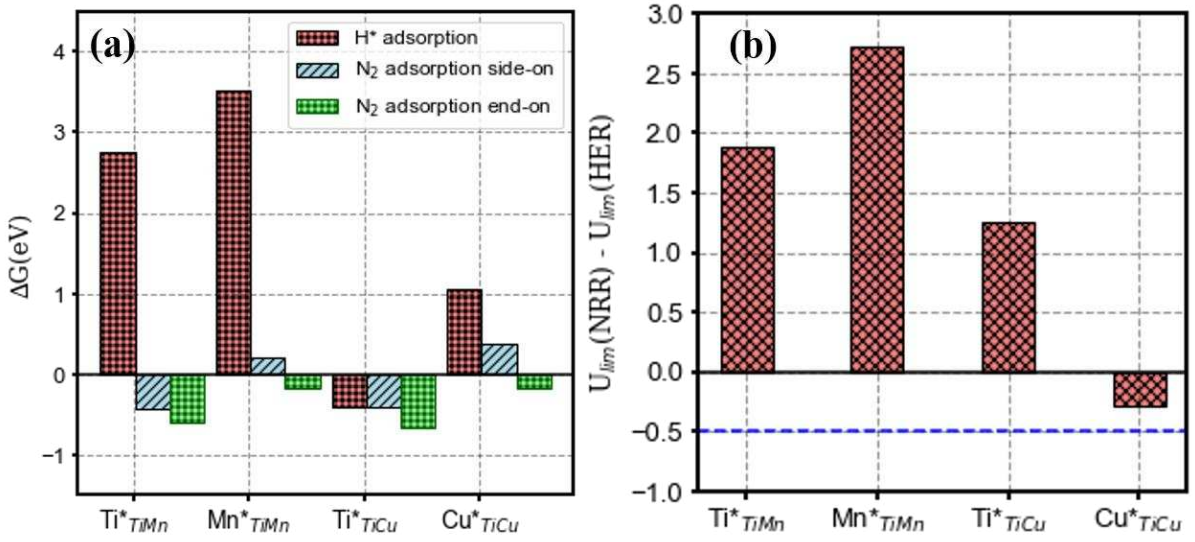

Figure 7. (a) The adsorption Gibbs free energy of $*N_2$ and *H adsorbed on Ti(Mn) and Ti(Cu) atom of $Ti_2Mn_4@C_{24}N_{24}$ and $Ti_2Cu_4@C_{24}N_{24}$ nanocages. (b) The difference in limiting potentials for NRR and HER at 0 V (vs. RHE). Dashed line: 0.5 V of the metal-based benchmark according to the reference [77].

To better understand the selectivity of the presented metal active sites of the two studied nanocages for NRR, the difference between the limiting potentials for the NRR and the HER on these catalysts are calculated following [93], i.e., $\Delta U = U_{lim}$ (NRR) – U_{lim}(HER). This indicates the dominance of NRR or HER on Ti (Mn) and Ti (Cu) atoms of $Ti_2Mn_4@C_{24}N_{24}$ and $Ti_2Cu_4@C_{24}N_{24}$ nanocages, respectively. As depicted in Figure 8b, the limiting potentials for NRR are more positive than those of HER on all active metal atoms except for the Cu center in $Ti_2Cu_4@C_{24}N_{24}$. In other words, the calculated free energy barriers of HER are much higher than those of the NRR, confirming that the NRR is more competitive than HER on all metal atoms of $Ti_2Mn_4@C_{24}N_{24}$ and $Ti_2Cu_4@C_{24}N_{24}$ (except the Cu atom in $Ti_2Cu_4@C_{24}N_{24}$). In addition, considering the metal-based benchmark of –0.5 V as a reference [77], one can see that the bimetal doped nanocages seem to have a higher selectivity for NRR than HER at 0 V

vs. RHE. Specifically, the selectivity for NRR follows the order of U_{lim} (NRR) − U_{lim}(HER) = 2.73 V > 1.88 V > 1.26 V > –0.29 V, for $Ti_2Mn_4@C_{24}N_{24}$ (Mn) > $Ti_2Mn_4@C_{24}N_{24}$ (Ti) > $Ti_2Cu_4@C_{24}N_{24}$ (Ti) > $Ti_2Cu_4@C_{24}N_{24}$(Cu), respectively.

Conclusion

We investigated the effects of various distribution patterns of doping two different single metal atoms into the pyridinic-N_4 cavities of $C_{24}N_{24}$ on its electrocatalytic activity using spin-polarized density functional theory (DFT) calculations. We found that the distribution patterns of bi-metal atoms into the pyridinic vacancies of porous $C_{24}N_{24}$ have a significant effect on the charge transfer, geometric and electronic properties of the catalyst, and therefore, its catalytic activity. Screening the electrocatalytic activity of $Ti_2Mn_4@C_{24}N_{24}$ and $Ti_2Cu_4@C_{24}N_{24}$ toward NRR at room temperature reveals that porous $C_{24}N_{24}$ acts as a suitable substrate to support Ti:Mn, and Ti:Cu metal atoms with a metal ratio of 2:4. Our results reveal that the Ti active sites on both catalysts have higher selectivity toward end-on N_2 adsorption and consequently the NRR than that on Mn and Cu centers. We confirmed theoretically that few-TM atom doped catalysts are promising for N_2 fixation and thus it is a good model to establish the structure-activity relationship. Our findings from the metal-N_4 moieties may help studies of related nanomaterials especially those with curved structures.

Acknowledgments

The authors gratefully acknowledge the financial support from the Fund of Scientific Research Flanders (FWO), Belgium, Grant number 1261721N. The computational resources and services used in this work were provided by the HPC core facility CalcUA of the Universiteit Antwerpen and VSC (Flemish Supercomputer Center), funded by the FWO and the Flemish Government.

References

[1] A. Klerke, C.H. Christensen, J.K. Nørskov, T. Vegge, Ammonia for hydrogen storage: challenges and opportunities, J. Mater. Chem., 18 (2008) 2304-2310.
[2] A. Vojvodic, A.J. Medford, F. Studt, F. Abild-Pedersen, T.S. Khan, T. Bligaard, J. Nørskov, Exploring the limits: A low-pressure, low-temperature Haber–Bosch process, Chem. Phys. Lett., 598 (2014) 108-112.
[3] A. Braun, D.K. Bora, L. Lauterbach, E. Lettau, H. Wang, S.P. Cramer, F. Yang, J. Guo, From inert gas to fertilizer, fuel and fine chemicals: N2 reduction and fixation, Catal. Today, (2021).
[4] J.R. Shah, F. Gorky, J. Lucero, M.A. Carreon, M.L. Carreon, Ammonia synthesis via atmospheric plasma catalysis: Zeolite 5A, a case of study, Ind. Eng. Chem. Res., 59 (2020) 5167-5176.
[5] S. Zheng, S. Li, Z. Mei, Z. Hu, M. Chu, J. Liu, X. Chen, F. Pan, Electrochemical nitrogen reduction reaction performance of single-boron catalysts tuned by MXene substrates, J. Phys. Chem. Lett., 10 (2019) 6984-6989.
[6] Z. Wei, Y. Zhang, S. Wang, C. Wang, J. Ma, Fe-doped phosphorene for the nitrogen reduction reaction, J. Mater. Chem. A, 6 (2018) 13790-13796.
[7] B. Ding, W.-J. Ong, J. Jiang, X. Chen, N. Li, Uncovering the electrochemical mechanisms for hydrogen evolution reaction of heteroatom doped M2C MXene (M= Ti, Mo), Appl. Surf. Sci., 500 (2020) 143987.
[8] K. Fan, Y. Jia, Y. Ji, P. Kuang, B. Zhu, X. Liu, J. Yu, Curved surface boosts electrochemical CO2 reduction to formate via bismuth nanotubes in a wide potential window, ACS Catal., 10 (2019) 358-364.
[9] H. He, C. Morrissey, L.A. Curtiss, P. Zapol, Graphene-supported monometallic and bimetallic dimers for electrochemical CO2 reduction, J. Phys. Chem. C., 122 (2018) 28629-28636.
[10] X. Cui, W. An, X. Liu, H. Wang, Y. Men, J. Wang, C 2 N-graphene supported single-atom catalysts for CO 2 electrochemical reduction reaction: mechanistic insight and catalyst screening, Nanoscale, 10 (2018) 15262-15272.
[11] Q. Shi, F. Peng, S. Liao, H. Wang, H. Yu, Z. Liu, B. Zhang, D. Su, Sulfur and nitrogen co-doped carbon nanotubes for enhancing electrochemical oxygen reduction activity in acidic and alkaline media, J. Mater. Chem. A, 1 (2013) 14853-14857.
[12] S. Kattel, G. Wang, A density functional theory study of oxygen reduction reaction on Me–N4 (Me = Fe, Co, or Ni) clusters between graphitic pores, J. Mater. Chem. A, 1 (2013).
[13] I.A. Amar, R. Lan, C.T. Petit, S. Tao, Solid-state electrochemical synthesis of ammonia: a review, Journal of Solid State Electrochemistry, 15 (2011) 1845.
[14] S. Giddey, S. Badwal, A. Kulkarni, Review of electrochemical ammonia production technologies and materials, Int. J. Hydrogen Energ., 38 (2013) 14576-14594.
[15] S. Ji, Z. Wang, J. Zhao, A boron-interstitial doped C 2 N layer as a metal-free electrocatalyst for N 2 fixation: a computational study, J. Mater. Chem. A, 7 (2019) 2392-2399.
[16] Q. Liu, S. Wang, G. Chen, Q. Liu, X. Kong, Activating graphyne nanosheet via sp-hybridized boron modulation for electrochemical nitrogen fixation, Inorganic chemistry, 58 (2019) 11843-11849.
[17] S. Sultana, S. Mansingh, K. Parida, Phosphide protected FeS 2 anchored oxygen defect oriented CeO 2 NS based ternary hybrid for electrocatalytic and photocatalytic N 2 reduction to NH 3, J. Mater. Chem. A, 7 (2019) 9145-9153.
[18] B. Cui, J. Zhang, S. Liu, X. Liu, W. Xiang, L. Liu, H. Xin, M.J. Lefler, S. Licht,

Electrochemical synthesis of ammonia directly from N 2 and water over iron-based catalysts supported on activated carbon, Green Chemistry, 19 (2017) 298-304.
[19] L. Yang, T. Wu, R. Zhang, H. Zhou, L. Xia, X. Shi, H. Zheng, Y. Zhang, X. Sun, Insights into defective TiO 2 in electrocatalytic N 2 reduction: combining theoretical and experimental studies, Nanoscale, 11 (2019) 1555-1562.
[20] X. Chen, N. Li, Z. Kong, W.-J. Ong, X. Zhao, Photocatalytic fixation of nitrogen to ammonia: state-of-the-art advancements and future prospects, Materials Horizons, 5 (2018) 9-27.
[21] J. Liu, Y. Liu, N. Liu, Y. Han, X. Zhang, H. Huang, Y. Lifshitz, S.-T. Lee, J. Zhong, Z. Kang, Metal-free efficient photocatalyst for stable visible water splitting via a two-electron pathway, Science, 347 (2015) 970-974.
[22] J. Zhu, Y. Wei, W. Chen, Z. Zhao, A. Thomas, Graphitic carbon nitride as a metal-free catalyst for NO decomposition, ChemComm, 46 (2010) 6965-6967.
[23] Y. Zheng, Y. Jiao, J. Chen, J. Liu, J. Liang, A. Du, W. Zhang, Z. Zhu, S.C. Smith, M. Jaroniec, Nanoporous graphitic-C3N4@ carbon metal-free electrocatalysts for highly efficient oxygen reduction, Journal of the American Chemical Society, 133 (2011) 20116-20119.
[24] J. Zhao, Z. Chen, Single Mo atom supported on defective boron nitride monolayer as an efficient electrocatalyst for nitrogen fixation: a computational study, Journal of the American Chemical Society, 139 (2017) 12480-12487.
[25] X. Guo, J. Gu, X. Hu, S. Zhang, Z. Chen, S. Huang, Coordination tailoring towards efficient single-atom catalysts for N2 fixation: A case study of iron-nitrogen-carbon (Fe@ NC) systems, Catal. Today, 350 (2020) 91-99.
[26] Z. Wei, Y. Feng, J. Ma, Co-doped graphene edge for enhanced N2-to-NH3 conversion, Journal of Energy Chemistry, 48 (2020) 322-327.
[27] P. Trogadas, T.F. Fuller, P. Strasser, Carbon as catalyst and support for electrochemical energy conversion, Carbon, 75 (2014) 5-42.
[28] K. Srinivasu, B. Modak, S.K. Ghosh, Porous Graphitic Carbon Nitride: A Possible Metal-free Photocatalyst for Water Splitting, J. Phys. Chem. C., 118 (2014) 26479-26484.
[29] J. Albero, A. Vidal, A. Migani, P. Concepción, L. Blancafort, H. García, Phosphorus-Doped Graphene as a Metal-Free Material for Thermochemical Water Reforming at Unusually Mild Conditions, ACS Sustainable Chemistry & Engineering, 7 (2018) 838-846.
[30] L. Li, L. Xu, Design of a graphene nitrene two-dimensional catalyst providing a well-defined site accommodating up to three metals, with application to N 2 reduction electrocatalysis, ChemComm, 56 (2020) 8960-8963.
[31] Z. Wei, J. He, Y. Yang, Z. Xia, Y. Feng, J. Ma, Fe, V-co-doped C2N for electrocatalytic N2-to-NH3 conversion, Journal of Energy Chemistry, 53 (2021) 303-308.
[32] Y. Pan, X. Liu, W. Zhang, Z. Liu, G. Zeng, B. Shao, Q. Liang, Q. He, X. Yuan, D. Huang, Advances in photocatalysis based on fullerene C60 and its derivatives: Properties, mechanism, synthesis, and applications, Appl. Catal. B-Environ., 265 (2020) 118579.
[33] F. Han, R. Wang, Y. Feng, S. Wang, L. Liu, X. Li, Y. Han, H. Chen, On demand synthesis of hollow fullerene nanostructures, Nat. Commun., 10 (2019) 1-9.
[34] A. Hayashi, Y. Xie, J.M. Poblet, J.M. Campanera, C.B. Lebrilla, A.L. Balch, Mass Spectrometric and Computational Studies of Heterofullerenes ([C58Pt]-,[C59Pt]+) Obtained by Laser Ablation of Electrochemically Deposited Films, J. Phys. Chem. A., 108 (2004) 2192-2198.
[35] P. Sood, K.C. Kim, S.S. Jang, Electrochemical Properties of Boron-Doped Fullerene Derivatives for Lithium-Ion Battery Applications, ChemPhysChem, 19 (2018) 753-758.
[36] J.P. Paraknowitsch, A. Thomas, Doping carbons beyond nitrogen: an overview of advanced heteroatom doped carbons with boron, sulphur and phosphorus for energy applications, Energy Environ. Sci., 6 (2013) 2839-2855.

[37] M.-A. Légaré, G. Bélanger-Chabot, R.D. Dewhurst, E. Welz, I. Krummenacher, B. Engels, H. Braunschweig, Nitrogen fixation and reduction at boron, Science, 359 (2018) 896-900.
[38] B. Gao, J.X. Zhao, Q.H. Cai, X.G. Wang, X.Z. Wang, Doping of calcium in C(60) fullerene for enhancing CO(2) capture and N(2)O transformation: a theoretical study, J. Phys. Chem. A., 115 (2011) 9969-9976.
[39] A.M. El Mahdy, Density functional investigation of CO and NO adsorption on TM-decorated C60 fullerene, Appl. Surf. Sci., 383 (2016) 353-366.
[40] T. He, A.R. Puente Santiago, A. Du, Atomically embedded asymmetrical dual-metal dimers on N-doped graphene for ultra-efficient nitrogen reduction reaction, J. Catal., 388 (2020) 77-83.
[41] C. Guo, T. Zhang, X. Liang, X. Deng, W. Guo, Z. Wang, X. Lu, C.-M.L. Wu, Single transition metal atoms on nitrogen-doped carbon for CO2 electrocatalytic reduction: CO production or further CO reduction?, Appl. Surf. Sci., 533 (2020).
[42] X. Gao, Y. Zhou, S. Liu, Z. Cheng, Y. Tan, Z. Shen, Single cobalt atom anchored on N-doped graphyne for boosting the overall water splitting, Appl. Surf. Sci., 502 (2020).
[43] T. Asset, P. Atanassov, Iron-Nitrogen-Carbon Catalysts for Proton Exchange Membrane Fuel Cells, Joule, 4 (2020) 33-44.
[44] P. Nematollahi, E.C. Neyts, Direct methane conversion to methanol on M and MN4 embedded graphene (M= Ni and Si): A comparative DFT study, Appl. Surf. Sci., 496 (2019) 143618.
[45] S. Liu, L. Cheng, K. Li, C. Yin, H. Tang, Y. Wang, Z. Wu, RuN4 Doped Graphene Oxide, a Highly Efficient Bifunctional Catalyst for Oxygen Reduction and CO2 Reduction from Computational Study, ACS Sustainable Chemistry & Engineering, 7 (2019) 8136-8144.
[46] K. Holst-Olesen, L. Silvioli, J. Rossmeisl, M. Arenz, Enhanced Oxygen Reduction Reaction on Fe/N/C Catalyst in Acetate Buffer Electrolyte, ACS Catal., 9 (2019) 3082-3089.
[47] Y. Jia, X. Xiong, D. Wang, X. Duan, K. Sun, Y. Li, L. Zheng, W. Lin, M. Dong, G. Zhang, Atomically Dispersed Fe-N 4 Modified with Precisely Located S for Highly Efficient Oxygen Reduction, Nano-Micro Letters, 12 (2020) 1-13.
[48] H.T. Chung, D.A. Cullen, D. Higgins, B.T. Sneed, E.F. Holby, K.L. More, P. Zelenay, Direct atomic-level insight into the active sites of a high-performance PGM-free ORR catalyst, Science, 357 (2017) 479-484.
[49] X. Wan, X. Liu, Y. Li, R. Yu, L. Zheng, W. Yan, H. Wang, M. Xu, J. Shui, Fe–N–C electrocatalyst with dense active sites and efficient mass transport for high-performance proton exchange membrane fuel cells, Nature Catalysis, 2 (2019) 259-268.
[50] A. Zitolo, N. Ranjbar-Sahraie, T. Mineva, J. Li, Q. Jia, S. Stamatin, G.F. Harrington, S.M. Lyth, P. Krtil, S. Mukerjee, Identification of catalytic sites in cobalt-nitrogen-carbon materials for the oxygen reduction reaction, Nat. Commun., 8 (2017) 1-11.
[51] S. Kattel, P. Atanassov, B. Kiefer, Density Functional Theory Study of Ni–Nx/C Electrocatalyst for Oxygen Reduction in Alkaline and Acidic Media, J. Phys. Chem. C., 116 (2012) 17378-17383.
[52] Z. Du, X. Chen, W. Hu, C. Chuang, S. Xie, A. Hu, W. Yan, X. Kong, X. Wu, H. Ji, Cobalt in Nitrogen-Doped Graphene as Single-Atom Catalyst for High-Sulfur Content Lithium–Sulfur Batteries, Journal of the American Chemical Society, 141 (2019) 3977-3985.
[53] W. Bi, X. Li, R. You, M. Chen, R. Yuan, W. Huang, X. Wu, W. Chu, C. Wu, Y. Xie, Surface Immobilization of Transition Metal Ions on Nitrogen‐Doped Graphene Realizing High‐Efficient and Selective CO2 Reduction, Adv. Mater., 30 (2018) 1706617.
[54] C. Zhang, J. Sha, H. Fei, M. Liu, S. Yazdi, J. Zhang, Q. Zhong, X. Zou, N. Zhao, H. Yu, Z. Jiang, E. Ringe, B.I. Yakobson, J. Dong, D. Chen, J.M. Tour, Single-Atomic Ruthenium Catalytic Sites on Nitrogen-Doped Graphene for Oxygen Reduction Reaction in Acidic

Medium, ACS Nano, 11 (2017) 6930-6941.
[55] E. Shakerzadeh, H. Hamadi, M.D. Esrafili, Computational mechanistic insights into CO oxidation reaction over Fe decorated C24N24 fullerene, Inorganic Chemistry Communications, 106 (2019) 190-196.
[56] A.A. Khan, M.D. Esrafili, R. Ahmad, I. Ahmad, Al-decorated C24N24 fullerene: A robust single-atom catalyst for CO oxidation, Polyhedron, 210 (2021) 115497.
[57] H. Hamadi, E. Shakerzadeh, M.D. Esrafili, A DFT study on the potential application of Si@ C24N24 porous fullerene as an innovative and highly active catalyst for NO reduction, Chem. Phys. Lett., 724 (2019) 80-85.
[58] J. Guo, Z. Liu, S. Liu, X. Zhao, K. Huang, High-capacity hydrogen storage medium: Ti doped fullerene, Appl. Phys. Lett., 98 (2011).
[59] C. Tang, S. Chen, W. Zhu, J. Kang, X. He, Z. Zhang, Transition metal Ti coated porous fullerene C24B24: potential material for hydrogen storage, Int. J. Hydrogen Energ., 40 (2015) 16271-16277.
[60] L.-J. Ma, W. Hao, T. Han, Y. Rong, J. Jia, H.-S. Wu, Sc/Ti decorated novel C24N24 cage: Promising hydrogen storage materials, Int. J. Hydrogen Energ., 46 (2021) 7390-7401.
[61] B. Modak, K. Srinivasu, S.K. Ghosh, Exploring metal decorated Porphyrin-like Porous Fullerene as catalyst for oxygen reduction reaction: A DFT study, Int. J. Hydrogen Energ., 42 (2017) 2278-2287.
[62] P. Nematollahi, E.C. Neyts, Linking Bi-Metal Distribution Patterns in Porous Carbon Nitride Fullerene to Its Catalytic Activity toward Gas Adsorption, Nanomaterials, 11 (2021) 1794.
[63] G. Kresse, J. Hafner, Ab initio molecular dynamics for liquid metals, Phys. Rev. B, 47 (1993) 558.
[64] J. Perdew, K. Burke, M. Ernzerhof, D. of physics and NOL 70118 J. quantum theory group tulane university, Phys. Rev. Lett, 77 (1996) 3865-3868.
[65] G. Kresse, J. Furthmüller, Efficiency of ab-initio total energy calculations for metals and semiconductors using a plane-wave basis set, Comput. Mater. Sci., 6 (1996) 15-50.
[66] P.E. Blöchl, Projector augmented-wave method, Phys. Rev. B, 50 (1994) 17953.
[67] J.P. Perdew, J.A. Chevary, S.H. Vosko, K.A. Jackson, M.R. Pederson, D.J. Singh, C. Fiolhais, Atoms, molecules, solids, and surfaces: Applications of the generalized gradient approximation for exchange and correlation, Phys. Rev. B, 46 (1992) 6671.
[68] S. Grimme, Semiempirical GGA‐type density functional constructed with a long‐range dispersion correction, J. Comput. Chem., 27 (2006) 1787-1799.
[69] R.T. Downs, M. Hall-Wallace, The American Mineralogist crystal structure database, American Mineralogist, 88 (2003) 247-250.
[70] W. Tang, E. Sanville, G. Henkelman, A grid-based Bader analysis algorithm without lattice bias, J. Phys. Condens. Matter, 21 (2009) 084204.
[71] X. Xia, G. Jones, M. Sarwar, Q. Tang, I. Harkness, D. Thompsett, A DFT study of Pt layer deposition on catalyst supports of titanium oxide, nitride and carbide, J. Mater. Chem. A, 3 (2015) 24504-24511.
[72] J.M. Hawkins, A. Meyer, T.A. Lewis, S. Loren, F.J. Hollander, Crystal structure of osmylated C60: confirmation of the soccer ball framework, Science, 252 (1991) 312-313.
[73] K. Srinivasu, S.K. Ghosh, Transition Metal Decorated Porphyrin-like Porous Fullerene: Promising Materials for Molecular Hydrogen Adsorption, J. Phys. Chem. C., 116 (2012) 25184-25189.
[74] Y.-D. Song, L. Wang, L.-M. Wu, How the alkali metal atoms affect electronic structure and the nonlinear optical properties of C24N24 nanocage, Optik, 135 (2017) 139-152.
[75] Z. Lu, G. Xu, C. He, T. Wang, L. Yang, Z. Yang, D. Ma, Novel catalytic activity for oxygen reduction reaction on MnN4 embedded graphene: A dispersion-corrected density

functional theory study, Carbon, 84 (2015) 500-508.
[76] E. Skulason, T. Bligaard, S. Gudmundsdóttir, F. Studt, J. Rossmeisl, F. Abild-Pedersen, T. Vegge, H. Jónsson, J.K. Nørskov, A theoretical evaluation of possible transition metal electro-catalysts for N 2 reduction, Phys. Chem. Chem. Phys., 14 (2012) 1235-1245.
[77] J.H. Montoya, C. Tsai, A. Vojvodic, J.K. Nørskov, The challenge of electrochemical ammonia synthesis: a new perspective on the role of nitrogen scaling relations, ChemSusChem, 8 (2015) 2180-2186.
[78] H. Niu, X. Wang, C. Shao, Z. Zhang, Y. Guo, Computational screening single-atom catalysts supported on g-CN for N2 reduction: High activity and selectivity, ACS Sustainable Chemistry & Engineering, 8 (2020) 13749-13758.
[79] Y. Cao, S. Deng, Q. Fang, X. Sun, C. Zhao, J. Zheng, Y. Gao, H. Zhuo, Y. Li, Z. Yao, Single and double boron atoms doped nanoporous C2N–h2D electrocatalysts for highly efficient N2 reduction reaction: a density functional theory study, Nanotechnology, 30 (2019) 335403.
[80] C.V.S. Kumar, V. Subramanian, Can boron antisites of BNNTs be an efficient metal-free catalyst for nitrogen fixation?–A DFT investigation, Phys. Chem. Chem. Phys., 19 (2017) 15377-15387.
[81] C. Ling, X. Niu, Q. Li, A. Du, J. Wang, Metal-free single atom catalyst for N2 fixation driven by visible light, Journal of the American Chemical Society, 140 (2018) 14161-14168.
[82] C. Liu, Q. Li, C. Wu, J. Zhang, Y. Jin, D.R. MacFarlane, C. Sun, Single-boron catalysts for nitrogen reduction reaction, Journal of the American Chemical Society, 141 (2019) 2884-2888.
[83] Y.-X. Lin, S.-N. Zhang, Z.-H. Xue, J.-J. Zhang, H. Su, T.-J. Zhao, G.-Y. Zhai, X.-H. Li, M. Antonietti, J.-S. Chen, Boosting selective nitrogen reduction to ammonia on electron-deficient copper nanoparticles, Nat. Commun., 10 (2019) 1-7.
[84] X. Yang, J. Nash, J. Anibal, M. Dunwell, S. Kattel, E. Stavitski, K. Attenkofer, J.G. Chen, Y. Yan, B. Xu, Mechanistic insights into electrochemical nitrogen reduction reaction on vanadium nitride nanoparticles, Journal of the American Chemical Society, 140 (2018) 13387-13391.
[85] X. Cui, C. Tang, Q. Zhang, A review of electrocatalytic reduction of dinitrogen to ammonia under ambient conditions, Advanced Energy Materials, 8 (2018) 1800369.
[86] C.J. Van der Ham, M.T. Koper, D.G. Hetterscheid, Challenges in reduction of dinitrogen by proton and electron transfer, Chem. Soc. Rev., 43 (2014) 5183-5191.
[87] X. Zhai, H. Yan, G. Ge, J. Yang, F. Chen, X. Liu, D. Yang, L. Li, J. Zhang, The single-Mo-atom-embedded-graphdiyne monolayer with ultra-low onset potential as high efficient electrocatalyst for N2 reduction reaction, Appl. Surf. Sci., 506 (2020) 144941.
[88] C. Ling, Y. Ouyang, Q. Li, X. Bai, X. Mao, A. Du, J. Wang, A General two‐step strategy‐based high‐throughput screening of single atom catalysts for nitrogen fixation, Small Methods, 3 (2019) 1800376.
[89] C. Choi, S. Back, N.-Y. Kim, J. Lim, Y.-H. Kim, Y. Jung, Suppression of hydrogen evolution reaction in electrochemical N2 reduction using single-atom catalysts: a computational guideline, ACS Catal., 8 (2018) 7517-7525.
[90] H.-J. Chun, V. Apaja, A. Clayborne, K. Honkala, J. Greeley, Atomistic insights into nitrogen-cycle electrochemistry: a combined DFT and kinetic Monte Carlo analysis of NO electrochemical reduction on Pt (100), ACS Catal., 7 (2017) 3869-3882.
[91] J.S. Anderson, J. Rittle, J.C. Peters, Catalytic conversion of nitrogen to ammonia by an iron model complex, Nature, 501 (2013) 84-87.
[92] Y. Abghoui, E. Skúlason, Onset potentials for different reaction mechanisms of nitrogen activation to ammonia on transition metal nitride electro-catalysts, Catal. Today, 286 (2017) 69-77.

[93] G. Qing, R. Ghazfar, S.T. Jackowski, F. Habibzadeh, M.M. Ashtiani, C.-P. Chen, M.R. Smith III, T.W. Hamann, Recent advances and challenges of electrocatalytic N2 reduction to ammonia, Chem. Rev., 120 (2020) 5437-5516.
[94] A. Singh, B. Rohr, J. Schwalbe, M. Cargnello, K. Chan, T. Jaramillo, 464 Chorkendorff, I.; Nørskov, JK, Electrochemical Ammonia Synthesis—The Selectivity Challenge. ACS 465, Catalysis, 7 (2017) 706-709.
[95] Z.W. Seh, J. Kibsgaard, C.F. Dickens, I. Chorkendorff, J.K. Nørskov, T.F. Jaramillo, Combining theory and experiment in electrocatalysis: Insights into materials design, Science, 355 (2017).
[96] H. Tao, C. Choi, L.-X. Ding, Z. Jiang, Z. Han, M. Jia, Q. Fan, Y. Gao, H. Wang, A.W. Robertson, Nitrogen fixation by Ru single-atom electrocatalytic reduction, Chem, 5 (2019) 204-214.

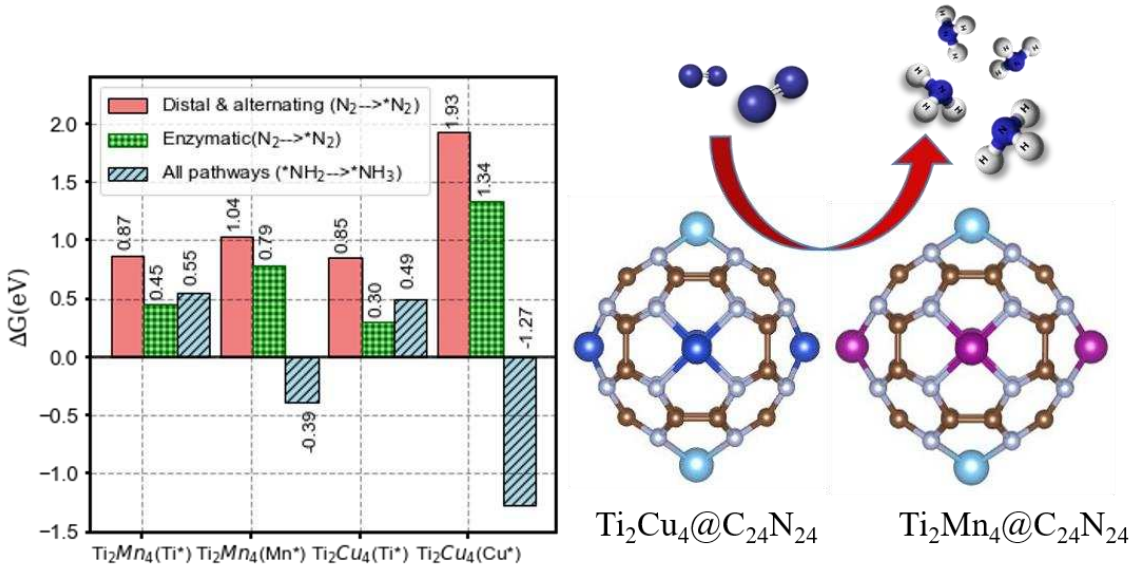

Graphic for Manuscript

Supporting information:

The distribution pattern of metal atoms in bi-metal doped pyridinic-N_4 pores determines their potential for electrocatalytic N_2 reduction

Parisa Nematollahi[*a], Erik C. Neyts[a]

[a] Research Group Plasmant, NANOlab Center of Excellence, Department of Chemistry, University of Antwerp, Universiteitsplein 1, 2610 Antwerp, Belgium

* Corresponding author. **Phone:** (+32) 32652346. **E-mail**: parisa.nematollahi@uantwerpen.be

Gibbs free energy computation details for NRR

Gibbs free energy (G) of the intermediates for the elementary steps of NRR ($N_2 + 6H^+ + 6e^- \rightarrow 2NH_3$) is calculated using the computational hydrogen electrode (CHE) model proposed by Nørskov et al [1-3]. In the CHE model, due to the constant charge constraint, the work function (or chemical potential) of the system changes from reactants to transition states (TSs) (or final states (FSs)) and fractional charge transfer is not allowed. In addition, the chemical potential of the H+/e^- pair in an aqueous solution is related to half of the H_2 gas molecule at the standard hydrogen electrode (SHE). In this method, the changes of the Gibbs free energy for each elementary step can be written as follows:

$\Delta G_n = \Delta E_n - T\Delta S + \Delta ZPE + \Delta G_{pH} + \Delta G_U$

Where ΔE_n refers to the reaction energy calculated by DFT calculations, T is the temperature (T=298.15 K). ΔZPE and ΔS are the difference in zero-point energy and entropy between the products and the reactants at room temperature which can be computed based on the vibrational frequencies. Notably, for the gas phase molecules, the entropy term can be obtained by the sum of the translational, rotational, and vibrational contributions, whereas only the vibrational modes of the adsorbed species are computed explicitly, and the surface of the catalyst is fixed by assuming that the vibrations of the solid surface are negligible. ΔG_{pH} refers to the correction of the H^+ free energy by the concentration: $\Delta G_{pH} = 2.303 \times k_B T \times pH$, where k_B is the

Boltzmann constant and the value of pH is set to be 0 for this work. ΔG_U is the free energy contribution related to the applied electrode potential (U) versus reversible hydrogen electrode (RHE), i.e., $\Delta G_U = -neU$, where n is the number of H+/e^- pairs transferred in NRR and e^- is the unit charge. The limiting potential (U_{lim}) is equal to the $-\Delta G_{max}/e^-$, where ΔG_{max} is the free energy change at the most uphill individual step i.e., the potential-determining step (PDS). Theoretical overpotential (η) is adopted as a measure for the whole NRR rate and is then determined as $\eta = U_{equ} - U_{lim}$, where U_{equ} is the equilibrium potential of NRR reaction, $N_2(g) + 6H^+ + 6e^- \rightarrow 2NH_3$ (aq) is +0.092 V vs. RHE, which is taken from the tabulated experimental standard reduction potentials [4, 5]. the smaller the η value the faster the N_2 reduction reaction. Note that the stabilization effects of water on the NRR is smaller than 0.10 eV per hydrogen bond [6, 7] previous theoretical studies have demonstrated that $*NH_2$ species is slightly more stable in the presence of water, while *N species will not be affected by the bulk water layer [8]. Therefore, considering the significant increase in the computational cost, an explicit solvent model for water was not used in this work.

Mechanisms of the NRR on $Ti_2Mn_4@C_{24}N_{24}$

NRR on Ti site.

Starting from the side-on N_2 adsorption configuration on the Ti active center of $Ti_2Mn_4@C_{24}N_{24}$, the probable NRR mechanism is the enzymatic pathway. Therefore, the first hydrogenation step (forming *N-*NH) is followed by alternating protonation of the two *N atoms (see Scheme 1). In this pathway, the two NH_3 molecules are released in the last two steps. As shown in Figure S1, the first hydrogenation step is a thermodynamically uphill step with ΔG = 0.45 eV. In the following exergonic step, the H^++e^- consecutively attacks the *N in *N-*NH species to form the *NH-*NH moiety with a free energy of -0.21 eV. Subsequently, in the third downhill protonation step, the *NH-*NH_2 produces. The formation of hydrazine, *NH-*NH_2 + (H^++ e^-) → *NH_2-*NH_2, is calculated to be the PDS with ΔG_{max} = 0.99 eV while the formation of the first NH_3 molecule is significantly exothermic, ΔG = -2.48 eV. Unlike the formation of the first NH_3 species, the second NH_3 produces by overcoming free energy of 0.55 eV. The onset potential of the enzymatic mechanism is calculated to be –0.99 V vs RHE.

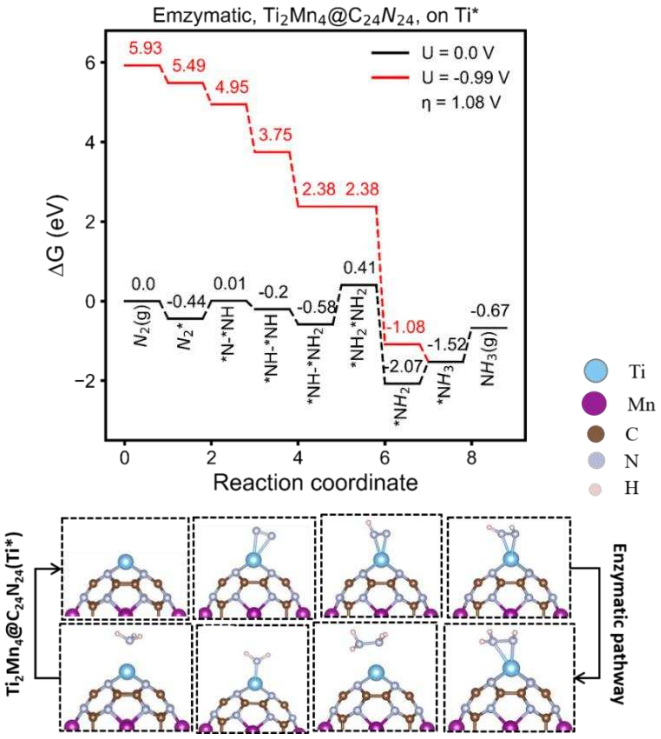

Figure S1. NRR via the enzymatic mechanisms on Ti site of $Ti_2Mn_4@C_{24}N_{24}$ along with the corresponding optimized configurations.

NRR on Mn site.

We then proceed to the NRR on the Mn atom of $Ti_2Mn_4@C_{24}N_{24}$. From the free energy diagram, we see that the protonation of $*N_2$ to *NNH is the rate-limiting step with a significantly high free energy of 1.04 eV. After the first hydrogenation step, the N-N bond length increases significantly from 1.13 Å in the adsorbed $*N_2$ form to 1.35 Å in the $*NNH_2$ configuration and releasing the first $*NH_3$ molecule leaving the N* atom on top of the Mn atom with the weak free energy of adsorption ΔG_{ads}=0.16 eV (see Figure S2a). In contrast to the distal pathway on the Ti site of $Ti_2Mn_4@C_{24}N_{24}$, the hydrogenation of $*NNH_2$ to *N is exothermic. The other hydrogenation steps are all downhill except for the formation of *NH intermediate which is slightly endothermic (ΔG = 0.22 eV).

Similar to the distal mechanism, the first hydrogenation of $*N_2$ to *N-*NH (ΔG_{max} =1.04 eV) in the alternating mechanism is considered the PDS (Figure S2b). The rest of the hydrogenation steps are downhill and spontaneous at room temperature except for the formation of diazene, *NH-*NH, which is slightly endothermic.

The computed overpotential in both pathways is calculated to be 1.13 V vs RHE. Therefore, we conclude that the NRR is not feasible on the Mn atom of $Ti_2Mn_4@C_{24}N_{24}$ via the distal and alternating pathways due to the significantly high onset potential and overpotential.

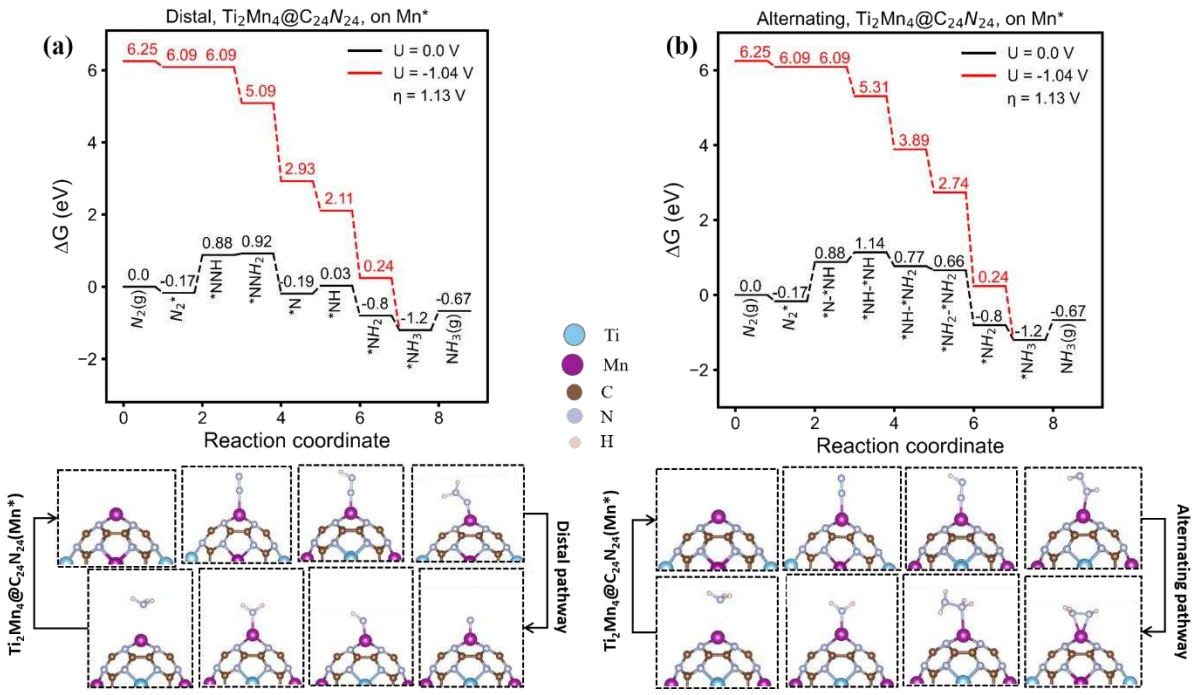

Figure S2. NRR via distal(a) and alternating (b) mechanisms on the Mn site of $Ti_2Mn_4@C_{24}N_{24}$ along with the corresponding optimized configurations.

Considering the side-on orientation for adsorbed N_2 on the Mn atom, the N_2 adsorption along with the first two hydrogenation steps are slightly endothermic. According to the computed free energies of all elementary steps in this pathway, we found that the hydrogenation of adsorbed $*N_2$ has the highest uphill energy and therefore is considered as the PDS with ΔG_{max} = 0.79 eV. Interestingly, the enzymatic mechanism outcompetes the other mechanisms for the NRR on the Mn atom of $Ti_2Mn_4@C_{24}N_{24}$. The calculated onset potential is −0.79 V vs. RHE which is in close agreement with that of MnN_4-G and Mn_3N_4-G with PDS equal to -0.68 V [9] and -0.69 V [10], respectively. Consequently, the computed overpotential is η = 0.88 V. However, unlike the Ti atom, N_2 molecule adsorbs via side-on configuration on the Mn sites with a low adsorption energy (ΔE_{ads} = -0.24 eV) and through a thermodynamically unfavorable reaction (ΔG_{ads} = +0.20 eV). Therefore, we estimate that the NRR is very unlikely to occur on the Mn centers of $Ti_2Mn_4@C_{24}N_{24}$.

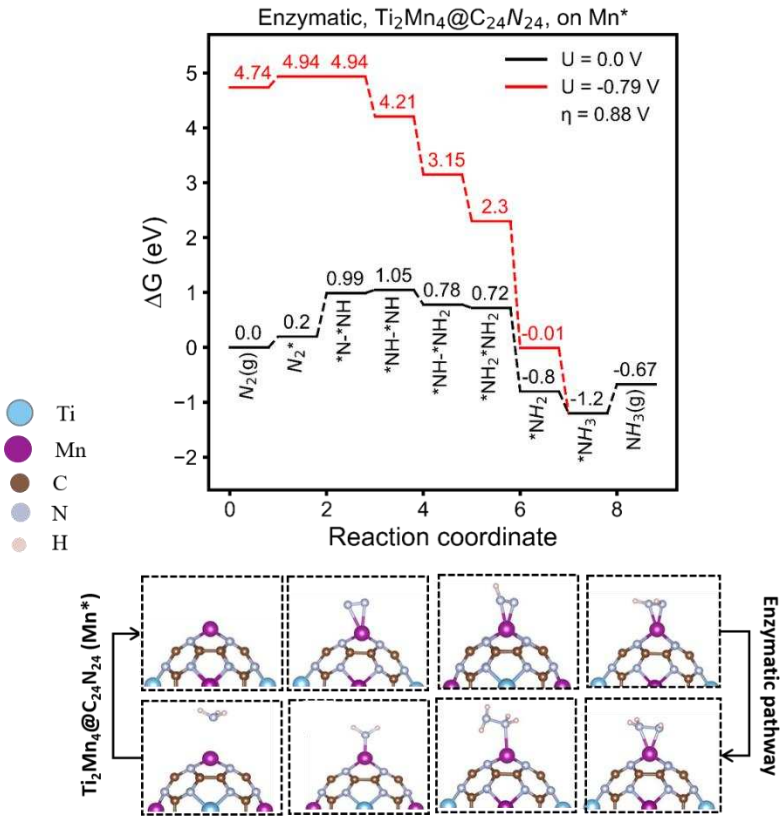

Figure S3. NRR via the enzymatic mechanisms on the Ti site of $Ti_2Mn_4@C_{24}N_{24}$ along with the corresponding optimized configurations.

Mechanisms of the NRR on $Ti_2Cu_4@C_{24}N_{24}$

NRR on Ti site.

When the NRR takes place along the enzymatic pathway, the first hydrogenation step, i.e., $*N_2 + (H^+ + e^-) \rightarrow$ *N-*NH, is uphill in the free energy profile by 0.30 eV in which the N-N bond length of the formed *N-*NH is elongated to 1.24 Å. The next hydrogenation steps in which the *NH-*NH and *NH-*NH_2 intermediates form, are thermodynamically feasible to occur under ambient conditions. The further hydrogenation of *NH-*NH_2 to form *NH_2-*NH_2 is somewhat difficult because it needs to overcome a free energy barrier of 0.97 eV. The approach of a fifth hydrogen leads to the dissociation of *NH_2-*NH_2 into *NH_2 and *NH_3, which is exothermic in the free energy profile by –2.43 eV, followed by the further hydrogenation of *NH_2 to the final product *NH_3 with the ΔG of 0.49 eV. As shown in Figure S4, we found that the PDS lies at the formation of hydrazine species with the onset potential of -0.97 V vs. RHE.

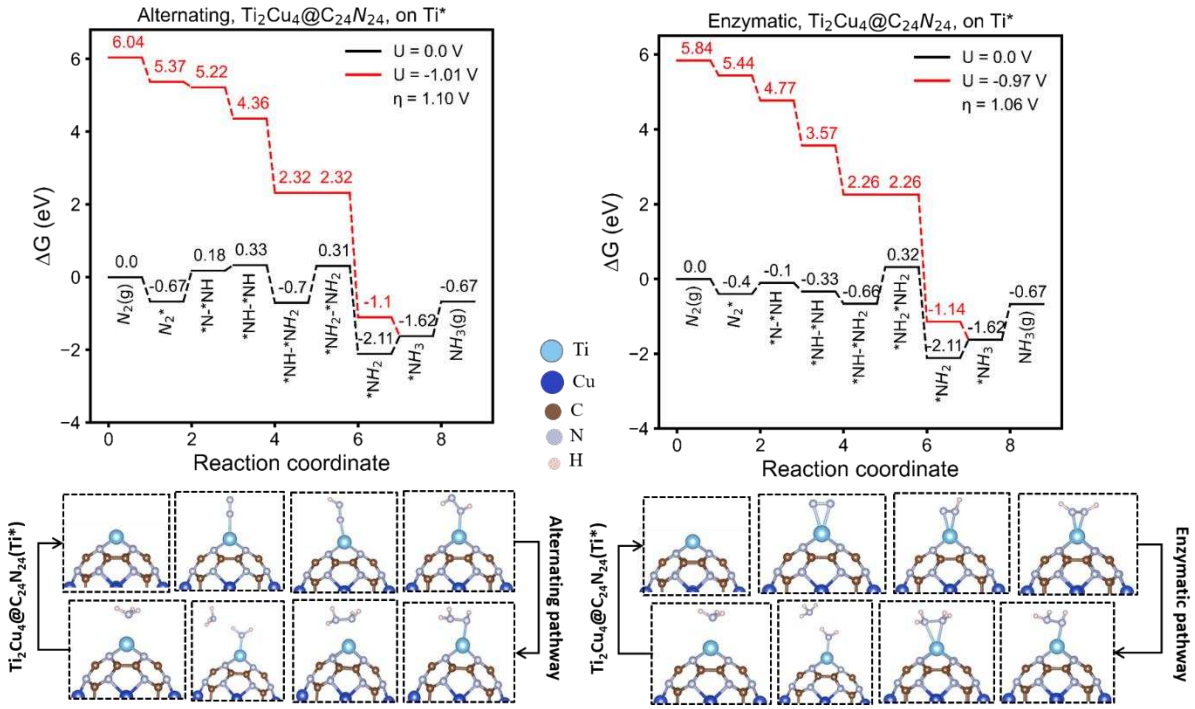

Figure S4. NRR via alternating (a) and enzymatic (b) mechanisms on the Ti site of $Ti_2Cu_4@C_{24}N_{24}$ along with the corresponding optimized configurations

NRR on Cu site.

In Figure 4, we showed that the Cu center of $Ti_2Cu_4@C_{24}N_{24}$ is not active for NRR due to the thermodynamically high free energy values required for the first hydrogenation of $*N_2$ species. To confirm this, we investigated the nitrogen hydrogenation steps through distal, alternating, and enzymatic pathways on the Cu atom. The corresponding reaction coordinates along with the optimized configurations are demonstrated in Figure S4. One can see that the highest ΔG_{max} for the NRR on the Cu atom of $Ti_2Cu_4@C_{24}N_{24}$ is attributed to the first protonation step with a significantly high free energy of ΔG_{max} = 1.93 eV for distal and alternating mechanisms and ΔG_{max} =1.34 eV for the enzymatic mechanism. Clearly, according to the high onset potential and consequently the high overpotential, we conclude that the NRR is not feasible on the Cu atom of $Ti_2Cu_4@C_{24}N_{24}$ catalyst at room temperature.

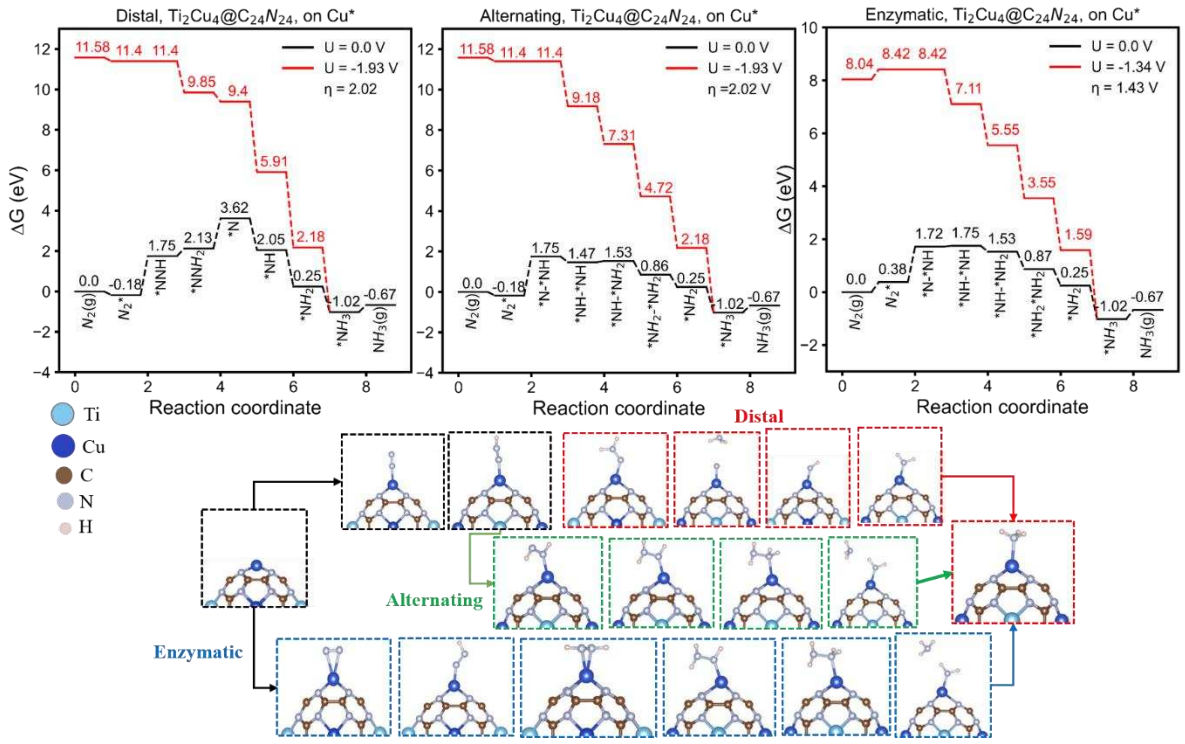

Figure S5. NRR via distal, alternating, and enzymatic mechanisms on Cu active site of $Ti_2Cu_4@C_{24}N_{24}$ along with the corresponding optimized configurations.

Table S1. The calculated Bader charges of doped TM atoms and adsorbed N_2 on each metal active site. All the charge values are in e.

Complex	$Ti_2Mn_4@C_{24}N_{24}$		$Ti_2Cu_4@C_{24}N_{24}$	
	Ti	Mn	Ti	Cu
Pure structure	+1.46	+1.26	+1.52	+0.84
N_2 (end-on)	-0.33	-0.20	-0.33	-0.16
N_2 (side-on)	-0.43	-0.34	-0.49	-0.14

Table S2. Calculated zero-point energies and entropy of different adsorption species on Ti/Mn and Ti atom of $Ti_2Mn_4@C_{24}N_{24}$ and $Ti_2Cu_4@C_{24}N_{24}$, respectively. * corresponds to the adsorption on the substrate.

Species	$Ti_2Mn_4@C_{24}N_{24}$ (Ti)		$Ti_2Mn_4@C_{24}N_{24}$ (Mn)		$Ti_2Cu_4@C_{24}N_{24}$ (Ti)	
	E_{ZPE} (eV)	TS (eV)	E_{ZPE} (eV)	TS (eV)	E_{ZPE} (eV)	TS (eV)
$*N_2$	0.18	0.14	0.16	0.20	0.18	0.19
*NNH	0.44	0.21	0.47	0.16	0.44	0.20
$*NNH_2$	0.77	0.19	-	-	0.78	0.24
*N	0.07	0.08	-	-	0.07	0.08
*NH	0.33	0.12	-	-	0.33	0.12
$*NH_2$	0.63	0.18	0.61	0.08	0.63	0.16
$*NH_3$	1.00	0.16	0.96	0.19	1.00	0.21
*NH*NH	-	-	0.75	0.15	-	-
$*NH*NH_2$	-	-	1.13	0.20	-	-
$*NH_2*NH_2$	-	-	1.46	0.22	-	-
*H	0.16	0.02	0.16	0.03	0.15	0.02

[1] A.A. Peterson, F. Abild-Pedersen, F. Studt, J. Rossmeisl, J.K. Nørskov, How copper catalyzes the electroreduction of carbon dioxide into hydrocarbon fuels, Energy Environ. Sci., 3 (2010) 1311-1315.
[2] Z. ValdØs, G.-J.K. Qu, J. Rossmeisl, JK Nørskov, J. Phys. Chem. C, 112 (2008) 9872-9879.
[3] J. Rossmeisl, Z.-W. Qu, H. Zhu, G.-J. Kroes, J.K. Nørskov, Electrolysis of water on oxide surfaces, Journal of Electroanalytical Chemistry, 607 (2007) 83-89.
[4] G. Qing, R. Ghazfar, S.T. Jackowski, F. Habibzadeh, M.M. Ashtiani, C.-P. Chen, M.R. Smith III, T.W. Hamann, Recent advances and challenges of electrocatalytic N2 reduction to ammonia, Chem. Rev., 120 (2020) 5437-5516.
[5] J. Deng, J.A. Iñiguez, C. Liu, Electrocatalytic nitrogen reduction at low temperature, Joule, 2 (2018) 846-856.
[6] V. Tripković, E. Skúlason, S. Siahrostami, J.K. Nørskov, J. Rossmeisl, The oxygen reduction reaction mechanism on Pt (1 1 1) from density functional theory calculations, Electrochim. Acta, 55 (2010) 7975-7981.
[7] Y. Abghoui, S.B. Sigtryggsson, E. Skúlason, Biomimetic nitrogen fixation catalyzed by transition metal sulfide surfaces in an electrolytic cell, ChemSusChem, 12 (2019) 4265-4273.
[8] E. Skulason, T. Bligaard, S. Gudmundsdóttir, F. Studt, J. Rossmeisl, F. Abild-Pedersen, T. Vegge, H. Jónsson, J.K. Nørskov, A theoretical evaluation of possible transition metal electro-catalysts for N 2 reduction, Phys. Chem. Chem. Phys., 14 (2012) 1235-1245.
[9] J. Xie, H. Dong, X. Cao, Y. Li, Computational insights into nitrogen reduction reaction catalyzed by transition metal doped graphene: Comparative investigations, Materials Chemistry and Physics, 243 (2020) 122622.
[10] G. Zheng, L. Li, Z. Tian, X. Zhang, L. Chen, Heterogeneous single-cluster catalysts (Mn3, Fe3, Co3, and Mo3) supported on nitrogen-doped graphene for robust electrochemical nitrogen reduction, Journal of Energy Chemistry, 54 (2021) 612-619.